Pressurised water flow in fractured permafrost rocks revealed by joint electrical resistivity monitoring and borehole temperature analysis

Maike Offer[1], Samuel Weber[2,3], Michael Krautblatter[1], Ingo Hartmeyer[4], and Markus Keuschnig[4]

[1]Chair of Landslide Research, Technical University of Munich, Munich, Germany
[2]WSL Institute for Snow and Avalanche Research SLF, Davos, Switzerland
[3]Climate Change, Extremes and Natural Hazards in Alpine Regions Research Center CERC
[4]GEORESEARCH, Puch bei Hallein, Austria

Correspondence: Maike Offer (maike.offer@tum.de)

Abstract. Rock slope instabilities and failures from permafrost are among the most significant alpine hazards in a changing climate and represent considerable threats to high-alpine infrastructure. While permafrost degradation is commonly attributed to rising air temperature and slow thermal heat propagation in rocks, the profound impact of water flow in bedrock permafrost on warming processes is increasingly recognized. However, quantifying the role of water flow remains challenging, primarily due to the complexities associated with direct observation and the transient nature of water dynamics in rock slope systems. To overcome the lack of quantitative assessment that inhibits thermal and mechanical modelling, we perform a joint analysis of electrical resistivity measurements and borehole temperature, combining datasets of monthly repeated electrical resistivity tomography acquired in 2013 and 2023, rock temperature measured in two deep boreholes (2016-2023), and site-specific temperature-resistivity relation determined in laboratory with samples from the study area. Field measurements were carried out at the permafrost-affected north flank of the Kitzsteinhorn (Hohe Tauern range, Austria), characterized by significant water outflow from open fractures during the melt season. Borehole temperature data demonstrate a seasonal maximum of the permafrost active layer of 4-5 m. They further show abrupt temperature changes ($\sim$ 0.2-0.7 °C) during periods with enhanced water flow, which cannot be explained by conductive heat transfer. Monthly repeated electrical resistivity measurements reveal a massive decrease in resistivity from June to July and the initiation of a low-resistivity ($<$ 4 kΩm) zone in the lower part of the rock slope in June, gradually expanding to higher rock slope sections until September. We hypothesize that the reduction in electrical resistivity of more than one order of magnitude, which coincides with abrupt changes in borehole temperature, provides certain evidence of pressurised water flow in fractures. This study shows for the first time that, in addition to slow thermal heat conduction, permafrost rocks are subject to sudden push-like warming events, favoring accelerated bottom-up permafrost degradation, and contributing to the build-up of hydrostatic pressures potentially critical for rock slope stability.

1 Introduction

Over the past decade, awareness of climate change-related hazards in alpine environments has increased, including the warming and thawing of permafrost. Degrading permafrost in rock walls can reduce the stability of rock slopes (Gruber and Haeberli,

2007), increasing the likelihood of slope failure and endangering mountain infrastructure (Duvillard et al., 2021b). Rising temperatures alter the mechanical properties of rock and ice (Krautblatter et al., 2013; Mamot et al., 2018), which can increase

25   the number of rockfalls and rock-slope failures in permafrost-affected rockwalls (Ravanel et al., 2017; Hartmeyer et al., 2020; Savi et al., 2021; Cathala et al., 2024). Therefore, precise knowledge of changes in frozen rock's thermal and mechanical regime is of particular interest to address mountain tourism's increased vulnerability and prevent or limit damage to high-alpine infrastructure (Duvillard et al., 2019).

Potential triggers of rock slope failure have been attributed to high water pressures (e.g., Fischer et al., 2010; Ravanel et al.,

30   2017; Walter et al., 2020) that can arise from the infiltration of rainwater or meltwater from snow, glaciers, ice-filled joints or permafrost. The infiltration capacity and hydraulic permeability of a rockwall are determined by the degree of fracturing, pore space characteristics, saturation, and temperature (Gruber and Haeberli, 2007). Ice-filled fissures reduce the permeability compared to unfrozen fissures (Pogrebiskiy and Chernyshev, 1977), leading to perched water and the build-up of high hydro-static pressures (Magnin and Josnin, 2021). Insitu observations of the internal hydrology of rockwalls remain scarce and often

35   difficult to implement. In ice-rich rock glaciers, piezometric measurements were used to investigate changes in water and ice content (Phillips et al., 2023; Bast et al., 2024). However, in the heterogeneous terrain of a rockwall, obtaining one-dimensional pressure data representative of the entire rockwall is challenging.

Non-conductive heat transport due to water flow along fractures can rapidly raise the temperature, leading to the formation of thaw corridors, which potentially enhance local permafrost degradation (Gruber and Haeberli, 2007) and erosion of ice-filled

40   clefts (Hasler et al., 2011) compared to slow thermal heat propagation in rocks. The physical processes of water flux in frozen bedrock are intrinsically difficult to quantify, exhibit non-linear, complex behavior, and are therefore poorly studied. Phillips et al. (2016) observed brief and intermittent thermal anomalies in borehole measurements in an alpine rock ridge, interpreted as water percolating through fractures after heavy precipitation. Seismic analysis and geophysical soundings have revealed seasonal variations in cleft-ice infill and meltwater percolation in fractures (Krautblatter et al., 2010; Keuschnig et al., 2017;

45   Weber et al., 2018).

Changes in water and ice content can be detected by electrical resistivity tomography (ERT), which is, therefore a well-established method (e.g., Hauck, 2002; Schneider et al., 2013; Hilbich et al., 2022; Cimpoiasu et al., 2024) that has been increasingly applied in mountain permafrost environments in recent years (Herring et al., 2023). Monitoring active layer dynamics and spatial and temporal permafrost evolution requires repeated ERT surveys, preferably using the same survey ge-

50   ometry and fixed installed electrodes. ERT monitoring over several years has demonstrated degrading permafrost associated with global warming (e.g., Mollaret et al., 2019; Scandroglio et al., 2021; Buckel et al., 2023). However, most monitoring approaches emphasize the inter-annual evolution of bedrock permafrost and often overlook seasonal variations in resistivity, especially during thawing periods.

ERT measurements offer valuable, indirect information, requiring either laboratory calibration (Krautblatter et al., 2010) or

55   ground temperature for quantitative interpretation. Borehole temperature measurements are direct thermal observations. They only provide point-scale data along the borehole profile in a heterogeneous alpine terrain but do not allow for differentiation between water and ice close to 0 °C. The freezing point of water can be shifted depending on rock properties, salinity, and pore

pressure (Arenson et al., 2022), allowing unfrozen water content at sub-zero temperatures. In addition, temperature changes may be slowed by latent heat effects while significant changes in the water-to-ice ratio occur. To reduce uncertainties in the
60 characterization of subsurface properties, a complementary approach that combines borehole observation and geophysical data such as electrical resistivity (e.g., Hauck, 2002; Etzelmüller et al., 2020) and/or seismic refraction data (e.g., Hilbich, 2010; Wagner et al., 2019) is required.

To address the lack of quantitative assessments of water flow in permafrost rockwall and the need to improve the understanding of rockwall hydrology (Krautblatter et al., 2012), we performed a unique combined analysis of repeated ERT measurements
65 and ground temperature from two deep boreholes (2016-2023) at the fractured north face of the Kitzsteinhorn (Hohe Tauern range, Austria). Compared to annual geoelectrical campaigns, our higher measurement frequency combined with long-term ground temperature data set allows us to investigate the complex seasonal water flow in permafrost rockwalls. This study underscores the importance of our integrated approach, emphasizing the significance of melt period analysis in delineating both temporal patterns and spatial distribution of intense water flow within fractures. Such insights are pivotal for accurate
70 interpretation and prediction of accelerated permafrost degradation and resulting rock slope instability.

2 Study site

The investigated rockwall is located in the summit region of the Kitzsteinhorn (3.203 m asl), part of the Hohe Tauern range in Austria (Fig. 1). The Kitzsteinhorn region is characterized by rocks of the Penninic Bündner Schist Formation in the Tauern Window and belongs to the Glockner Nappe. The lithology in the study area is dominated by calcareous mica-schists traversed
75 by a scaly band of serpentinite parallel to the schistosity that dips steeply with approximately 45° to NNE (Cornelius and Clar, 1935; Hoeck et al., 1994; Hartmeyer et al., 2020).

The north face of the Kitzsteinhorn exhibits a significant degree of fracturing, characterized by joint openings of up to 20 cm, predominantly along cleavage planes (Schober et al., 2012). The development of the enormous number of joint sets was favored by stress release and intense physical weathering processes (Hartmeyer et al., 2012). The main joint sets are K1,
80 which has a sub-vertical dip to the west, and K2, which features a steep dip to the southwest (Fig. 1). K3 and K4 are less abundant. K3 dips medium-steeply to flat to S-SSE, and K4 dips steeply to NW. Laboratory tests of mica-schist rocks with ice-filled joints have shown that the shear resistance along rock-ice interfaces follows a temperature- and stress-dependent failure criterion, where warming and unloading lead to a mechanical destabilization and can lead to self-enforced rock slope failure (Mamot et al., 2020). Keuschnig et al. (2017) installed 2012 the ERT profile at the north-facing rockwall below the station of
85 the Kitzsteinhorn cable car, ranging from an elevation of 2.965 to 3.017 m asl (Fig. 1). The flank has been severely affected at its base by the rapid retreat of the Schmiedingerkees Glacier, which caused increased rockfall activity in the lower part of the rockwall, with single detachments of up to 880 m^3 (Hartmeyer et al., 2020). Several rockfall events have damaged the lower part of the ERT profile. As a result, the electrical resistivity measurements, carried out monthly from June to September 2023, now cover an elevation range from 2.976 to 3.017 m asl (Fig. 2). The slope gradient of the rock face increases as it approaches
90 the glacial cirque and is averaged at 47° (Keuschnig et al., 2017).
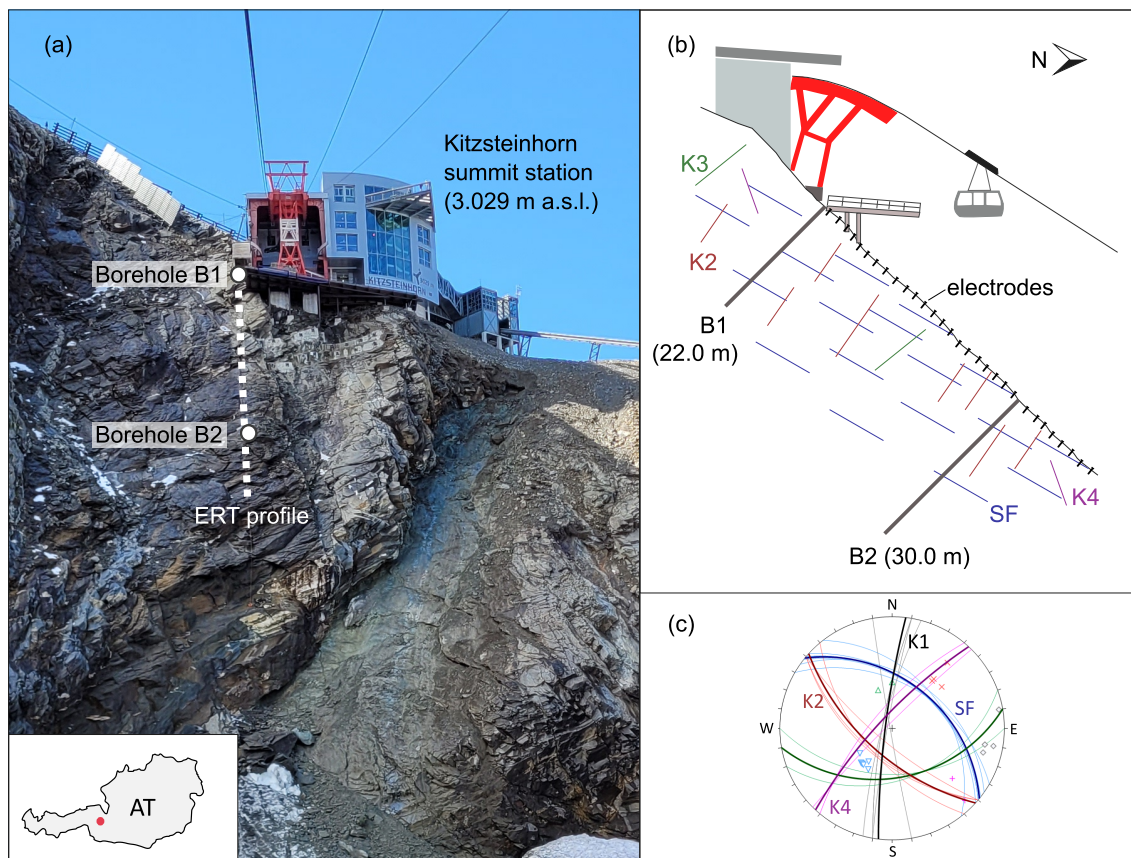
Figure 1. (a) Detailed view of the investigated, north faced rockwall below the Kitzsteinhorn summit station (Hohe Tauern range, Austria), the position of the ERT profile, and the two deep boreholes B1 and B2. (b) The geotechnical setting of the rock face is described by the schematic representation of the main discontinuities K1, K2, K3, K4, and the schistosity SF, as well as (c) the dip angle and direction of their mean set planes.

This study is part of the 'Open-Air-Lab Kitzsteinhorn' (Keuschnig et al., 2011; Hartmeyer et al., 2012), a comprehensive long-term project to monitor the response of bedrock permafrost to climatic change across multiple scales. Empirical-statistical calculations by Schrott et al. (2012) on the distribution of permafrost in the Hohe Tauern region indicate a high permafrost probability above 2.500 m asl on north-facing rockwalls and above 3.000 m asl on south-facing slopes of the Kitzsteinhorn.

95 In addition, permafrost has been detected by electrical resistivity measurements in the northern section of the tunnel 'Hannah-Stollen', which connects the Kitzsteinhorn cable car station to the south side at an elevation of approximately 3.000 m asl (Hartmeyer et al., 2012).
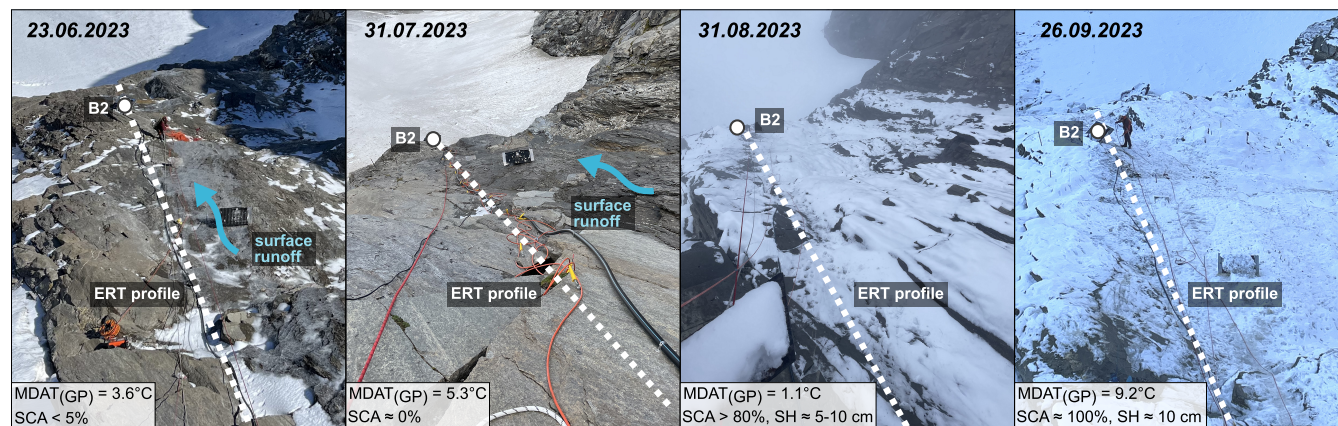
Figure 2. Weather and rock surface conditions on the days of ERT measurements in 2023 described by mean daily air temperature (MDAT) derived from the nearby ($\sim$ 500 m distance) weather station at the Glacier Plateau (GP), and estimated values of snow cover area (SCA) and snow height (SH). During the ERT measurements in June and July, pronounced surface runoff was observed in the lower part of the ERT profile.

3 Methods and data processing

3.1 Laboratory calibration of temperature-resistivity relation

100 The temperature-resistivity relation was derived from laboratory experiments of seven cylindrical samples ($\varnothing$ = 80 mm) drilled from four calcareous mica-schist rock samples from the study side. The core samples were saturated for several weeks with tap water. At the chemical equilibrium ($\sim$ 17 °C), water conductivity was 0.058 ± 0.002 S m^{-1}. Full saturation of pore spaces was achieved under atmospheric pressure, as applying a vacuum would result in higher water absorption, which is less representative of field conditions (Krus, 1995; Sass, 1998). However, the free saturation method is likely subject to the

105 occurrence of air bubbles (Draebing and Krautblatter, 2012), which may complicate the interpretation of the results.

Figure 3a illustrates the experimental setup for the laboratory electrical resistivity measurements. Two copper plates were placed on the grounded end-faces of the samples as current electrodes (A and B). For the voltage electrodes (M and N), copper pipe clamps were installed around the core sample with equal spacing between the electrodes. Pressure was applied to the current electrodes to ensure good electrical contact. Resistivity ρ was calculated from the cross-section of the core sample A,

110 the applied voltage V, the distance between the voltage electrodes L, and the resulting current I (Telford et al., 2004):

$$\rho = \frac{AV}{LI} \tag{1}$$

Temperature of the core samples was controlled by a freezing chamber which can be regulated in 0.1 °C increments. The rock samples were slowly warmed from -3 to 3 °C with a gradient of 0.3 °C h^{-1} to ensure temperature homogeneity. To avoid electrical interference, rock temperature was measured on a second, characteristically identical sample at depths of 25 and

115 40 mm with two thermometers (Greisinger GMH 3750, with 0.1 °C accuracy GTF 401 sensors). The samples were loosely
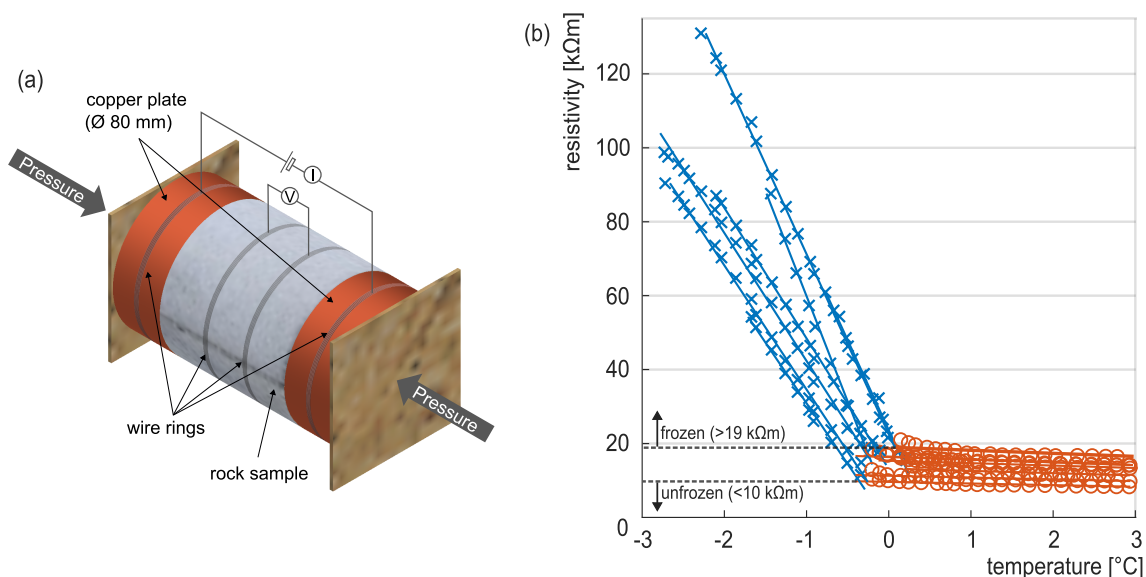
Figure 3. (a) Simplified schematic illustrating the setup of the laboratory calibration. (b) Temperature-resistivity relation of laboratory experiments of seven mica-schist core samples indicating unfrozen conditions under 10 kΩm and frozen conditions above 19 kΩm.

covered with plastic film and ventilated to prevent drying and thermal layering. According to the field investigations, continuous resistance measurements were done with ABEM terrameter LS using a minimum current of 0.1 mA and a maximum voltage output of 600 V.

3.2 ERT data acquisition

120 ERT is a non-invasive geophysical method for detecting and monitoring the distribution and properties of permafrost: an electric current is injected into the subsurface by two electrodes, and the resultant electrical potential difference is measured at two other electrodes. The respective apparent resistivity of the electrical field is then determined by the injected current, the measured potential difference, and a geometric factor. The investigation depth depends on the electrode spacing, with shorter spacing resulting in a lower depth of investigation but higher resolution near the surface. The apparent resistivity values need

125 to be inverted using an appropriate algorithm to provide areal information on the electrical resistivity distribution. Ice-filled joints and frozen or dry bedrock are typically characterized by high electrical resistivity, whereas unfrozen conditions and high liquid water content are associated with low electrical resistivity (Hauck, 2002). The ERT profile used for the present study was installed in 2012 and initially used for a year-long continuous subsurface monitoring of permafrost conditions using automated ERT starting in February 2013 (Keuschnig et al., 2017). Therefore, 37 electrodes were permanently drilled into the bedrock at

130 intervals of 2 m. To improve the electrical contact with the bedrock and ensure long-term durability, stainless-steel climbing bolts with a length of 90 mm and a diameter of 10 mm were preferred to fixed stainless-steel screws (Krautblatter and Hauck, 2007). The automated ERT measurements were performed from February-December 2013 on a 4-hour sampling interval using

Wenner configuration, as it provides the best signal-to-noise ratio in permafrost rockwalls (Zhou and Dahlin, 2003) and good horizontal resolution (Hauck and Kneisel, 2008). Two lightning strikes severely damaged the hardware and prevented most

135 measurements between June and September 2013. We performed ERT measurements over a 24-hour period at the end of each month from June to September 2023 using the same protocol type to fill this data gap. We analyzed short-term variations in electrical resistivity values for each measurement campaign to exclude random errors and quantify the respective measurement uncertainty (Fig. B1). Due to several rockfall events, the lower part of the ERT profile was damaged, and only the top 30 fixed electrodes could be used in 2023. To enable comparison of the 2013 and 2023 data series on a temporal and spatial scale, we

140 selected representative tomographies at the end of each month of the automated ERT measurements in 2013 (February-June and September-December) and shortened them to the same profile length (electrodes 1-30). Further technical details of the respective ERT measurements are given in Table B1.

The ERT measurements conducted in 2023 were carried out under varying weather conditions (Fig. 2). A thin layer of ice partially covered the rock surface during the morning and night of the ERT measurements in June, while significant surface

145 runoff was observed passing the lower part of the ERT profile during the afternoon of the June campaign and throughout the measurement period in July. During ERT observations in August and September, most of the rockwall was covered by snow, reaching a height of up to 10 cm. Mean daily air temperature derived from a nearby weather station on the Glacier Plateau (distance $\sim$ 500 m, 2.940 m asl) indicated positive values for all days of ERT measurements in 2023.

Datum points with considerable deviations from neighboring values were manually filtered, resulting in a maximum dec-

150 laration of 2 % of datum points per measurement. These outliers were masked and excluded from further data processing. All ERT measurements were inverted using the software package Res2Dinv (Loke and Barker, 1996) with adapted settings for permafrost rock faces. Robust inversion routines with half electrode spacing and mesh refinement were applied to cope with expected high electrical resistivity gradients (Krautblatter and Hauck, 2007). After four to five iterations, a reasonable level of convergence was achieved without over-fitting the data. Resistivity models with a high root mean square (RMS) error

155 between the modelled and observed data are obtained, particularly during the winter months when frozen surface conditions impede the coupling of electrodes. However, an assumption of inaccuracy and subsequent complete exclusion of the affected data sets only justified by a high RMS error is inappropriate. We, therefore, retained the data sets of the winter measurements but withheld detailed interpretation in recognition of the potential presence of noise. In addition, the change in the raw data, i.e. the apparent resistivity, of the different measurements was analysed in relation to the investigation depths to exclude artifacts

160 from the inversion (Fig. B2). A summary of the data post-processing is given in Table B1.

3.3 Borehole temperature measurements

Rock temperature measurements in two deep boreholes close to the geoelectrical profile have been conducted since December 2015. Borehole B1 is situated close to electrode 1 (x = 0 m) at an elevation of 3.030 m asl, and borehole B2 is positioned between electrodes 22 (x = 42 m) and 23 (x = 44 m) at an elevation of 2.970 m asl. Both boreholes were drilled perpendic-

165 ular to the surface and the schistosity, reaching a depth of 22 m (B1) and 30 m (B2). The temperature inside both boreholes was recorded based on a highly sensitive measuring system: After drilling, B1 and B2 were equipped with water- and airtight

polyethylene casings interrupted by non-corrosive brass rings at the designated depths of the temperature sensors. The annulus was filled with concrete to avoid water/air circulation and ice formation in the void between the casing and ambient bedrock. A chain of customized high-precision Pt100 thermistors (accuracy ± 0.03 °C) was inserted into the casing and established direct mechanical contact with the brass rings of the casings. Due to the high thermal conductivity of the brass rings and their direct physical connection to the sensors, this setup enables improved thermal coupling between the temperature sensor and surrounding rock mass compared to most other systems. The system used for the present study thus responds sensitively to (minor) changes in temperature and is well-suited to record short-term fluctuations of bedrock temperature. Sensors were installed at 0.1, 0.5, 1, 2, 3, 5, 7, 10, 15, 20, 21.5 (only B1), 25 (only B2) and 30 m (only B2) depth. The measuring interval was set to 10 minutes. Scaled images of the borehole walls were acquired using an optical scanner to identify and locate discontinuities. These images provided insight into parameters including joint frequency and aperture over the entire depth of B1 (22 m) and to a depth of approximately 15 m in B2.

Lightning strikes damaged several thermistors throughout the long-term monitoring (2016-2023), leading to data gaps starting in June 2017 (B2 = 0.5, 10 m), July 2019 (B2 = 20 m), June 2020 (B2 = 7 m), September 2020 (B2 = 25 m), April 2023 (B1 = 20 m), June 2023 (B1 = 7, 10, 21.5 m, B2 = 1 m). Warming releases resulting from construction activities in summer 2023, mainly due to drilling operations near B1, could have affected ground temperature measurements. Consequently, we excluded the affected data sets from B1 (August-December 2023).

4 Results

4.1 Temperature-resistivity laboratory calibration

Figure 3b shows the rock temperature related to the measured electrical resistivity of the laboratory analysis. Warming of the frozen rock samples (n = 7) starting at −3 °C followed a linear temperature-resistivity behavior with a steep gradient of −44.9 ± 12.0 kΩm/ °C up to the equilibrium melting point between −0.4 and 0.2 °C. The resistivity values at the equilibrium melting point ranged from 10-19 kΩm, which is subsequently used as a threshold for the transition zone between frozen and unfrozen conditions for the inverted tomograms of the Kitzsteinhorn rock face. The unfrozen temperature-resistivity paths exhibit a flatter gradient of −0.6 ± 0.2 kΩm/ °C. The fitting parameters and respective R^2 of the curves are listed in Table A1.

4.2 Seasonal variations in ERT

The seasonal evolution of the ERT acquired from February-June 2013, June-September 2023, and September-December 2013 are shown in Fig. 4. In February, resistivity values greater than 64 kΩm were observed throughout the profile except for a small area of measurement noise (electrode 24-25). Only slight decreases in resistivity occurred in March 2013 and April 2013 at depths between 5 and 10 m, as well as at shallower depths in April 2013, June 2013, and June 2023. Nevertheless, electrical resistivity values remained above 32 kΩm, indicating frozen rock and ice-filled joints. Borehole temperature data from B2 (Fig. 5a) suggests an active layer thickness of approximately 1.7 m at the time of the ERT measurement in June 2023, which is
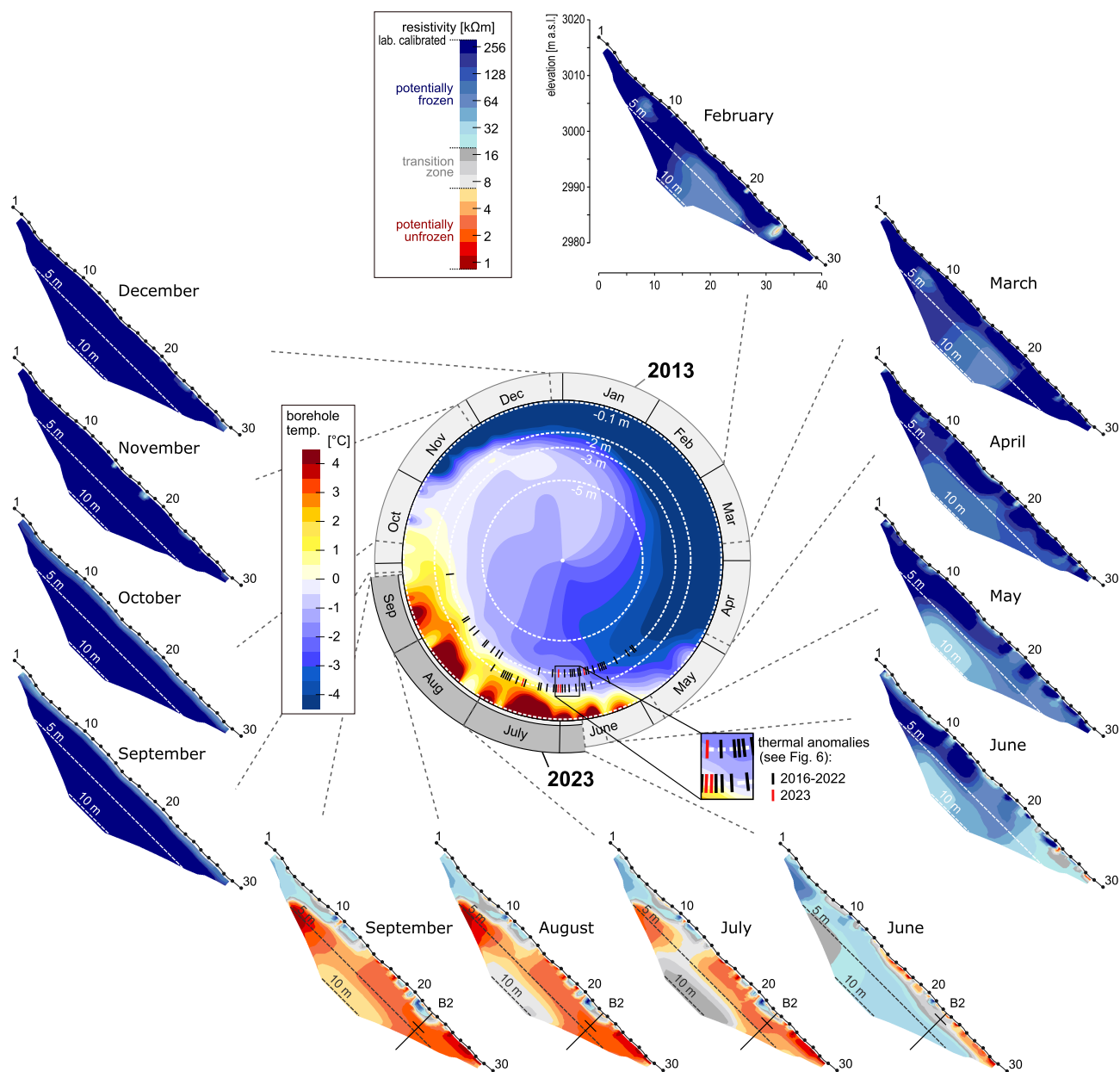
Figure 4. Tomographies of repeated ERT measurements from February to June 2013, June to September 2023, and September to December 2013, revealing seasonal resistivity changes. The position of borehole B2 is indicated in the resistivity profiles 2023, with horizontal lines representing the 0°C threshold at the date of the ERT measurements. The central polar plot illustrates rock temperature recorded in borehole B2 from January-December 2023, indicating measurement depths by dashed lines. Thermal anomalies (abrupt temperature changes) found in both boreholes over the entire observation period (2016-2023) are marked at the respective time and depth.

in good agreement with near-surface ($\sim$ 0-2 m depth) electrical resistivity values of less than 12 kΩm in the lower part of the tomography ($\sim$ electrodes 15-30). The most pronounced seasonal variation in electrical resistivity occurs in summer (Fig. B1). In July, the low-resistivity zone in the lower part of the tomography expands to $\sim$ 5 m depth while resistivity drops to around 4 kΩm. In July and August, this trend continues as the low-resistivity zone extends to the bottom of the tomography ($\sim$ 10 m depth). The upper part of the profile ($\sim$ electrodes 1-10) is unaffected by the trend. A high resistivity body of $\geq$ 32 kΩm remains stable during the summer month, probably due to the shielding of water infiltration through the cable car station combined with an intact rock mass without major fractures. Coinciding with the freezing period from September to December 2013, high electrical resistivity values reappeared ($\geq$ 128 kΩm).

The general shift towards lower resistivity values from June to September is also clearly discernible in the raw data (Fig. B2). The median values of the apparent resistivities decreased from 15.6 kΩm in June 2023 to 5.5 kΩm in July and remained at low levels from August (4.0 kΩm) to September (3.4 kΩm). Pre-processed data from ERT measurements in June (2013 and 2023) show comparable characteristics with a wide range of apparent resistivity values and a reasonable number of data points above 19 kΩm (i.e., laboratory threshold of frozen conditions). From July to September, apparent resistivities greater than 19 kΩm occurred sporadically at shallow depths, whereas values characteristic for unfrozen conditions (< 10 kΩm) are more pronounced and were observed solely in deep-penetrating measurements.

4.3 Borehole temperature and thermal anomalies

The polar plot in the center of Fig. 4 shows a one-year bedrock temperature cycle measured in B2 from January to December 2023. Rock temperature at depth shows a delayed and damped response to cooling and warming. At B2, for instance, a temperature maximum at 5 m was recorded in late December (−0.6 °C) while the minimum was registered in early May (−3.4 °C). The zero-curtain effect, i.e., an isothermal state where rock temperature stagnates close to 0 °C due to the release of latent heat (Outcalt et al., 1990), was most pronounced at 3 m depth in B2.

Interpolated borehole temperature records from ERT measurement days in 2023 indicate subzero subsurface conditions below depths of 0.5 m (B1) and 1.7 m (B2) in June, 3.3 m (B1) and 2.7 m (B2) in July, 3.4 m in August (B2), and 3.5 m in September (B2), see Fig. 5a. The annual variations in ground temperature as well as the characteristic parameters of active layer thickness (ALT), depth of zero annual amplitude (DZAA), and thermal offset were calculated for B2 for 2023, while for B1, the year before construction activities (August 2022-July 2023) was analyzed. The seasonal maximum of the ALT was reached at a depth of 4.3 m in B1 and of 3.9 m in B2; the DZAA, defined by the annual temperature amplitude of less than 0.1 °C (Gruber et al., 2004), was only reached in B2 at around 28.4 m. The thermal offsets, calculated by the difference between the annual mean ground temperature at 0.1 m depth and the mean annual temperature at the top of the permafrost, demonstrate positive values (B1 = 1.5 °C, B2 = 0.9 °C) due to an increasing mean annual ground temperature from the surface to the permafrost table.

The quasi-sinusoidal temperature curves recorded over the observation period at 2, 3, 5, 10, and 15 m depth suggest that heat transport in the intact rock mass is dominated by conduction (Fig. 6). Nonetheless, borehole temperature showed 69 abrupt changes (thermal anomalies) at 2 and 3 m depth (B1, B2), which were identified using the first derivative with a moving
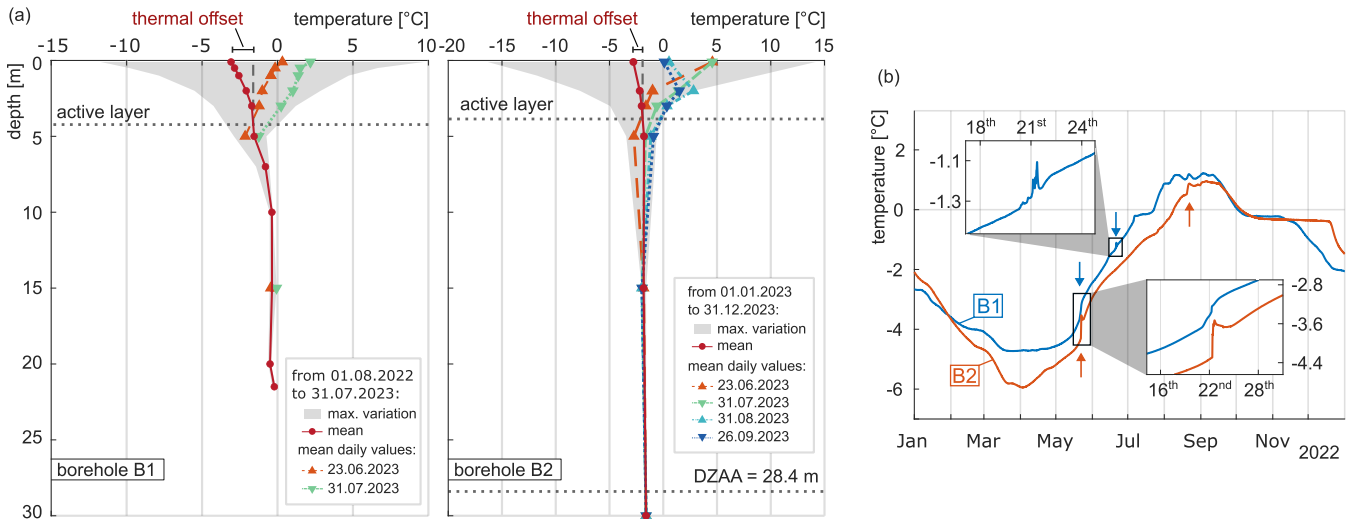
Figure 5. (a) Ground temperature in boreholes B1 and B2 at the ERT measurement days from June to September 2023. The maximum annual variation of the ground temperature, the thickness of the active layer, the depth of zero annual amplitude (DZZA), and the mean annual ground temperature were determined for representative periods, respectively (B1: the year before construction activities started in August 2023, B2: the year 2023). (b) Thermal anomalies (abrupt temperature changes) found in the borehole temperature data, exemplified by the record taken at 3 m depth from 2022.

average of 12 data points (i.e., measurement interval of 2 hours, Fig. 6) and were manually reviewed for characteristics typical of non-conductive heat transfer (i.e., temperature rise of $\sim$ 0.2-0.7 °C in less than 2-4 hours, Fig. 5b). Sudden, significant changes between two measurements (10 min) with a return to the previous temperature level are caused by overvoltage effects

235 following lightning strikes and were therefore not considered further. In addition, gradient changes after the zero-curtain effect were also filtered out. Near-surface temperatures (depth < 2 m) were excluded from the analysis as they are characterized by short-term fluctuations with large amplitudes, making distinguishing between changes induced by non-conductive heat transfer and meteorologically forced changes complex. Borehole temperatures at greater depths from 5-30 m are likely less sensitive to heat transfer from percolating water, but exhibited 13 irregularities at 5 m depth (B1, B2) and notable changes

240 in the quasi-sinusoidal pattern since 2020 at 10 and 15 m depth (B1). All abrupt changes and irregularities in the borehole temperature occurred between late May and September, coinciding with the significant decrease in resistivity observed in the ERT measurements from June to September (Fig. 4).

Optical borehole imaging shows a pronounced occurrence of clefts with apertures of up to 5 cm in the first ten meters in B1 and B2 and intact rock mass of calcareous mica-schist with marked schistosity at greater depths (Fig. 6). Thermistors

245 installed close or within clefts or areas of schistosity exhibit a higher frequency of thermal anomalies, as evidenced by the counts recorded (e.g., B1-2 m: 18, B2-3 m: 25), in contrast to thermistors installed at a greater distance, not exceeding 50 cm, from discontinuities (B2-2 m: 10, B1-3 m: 16).
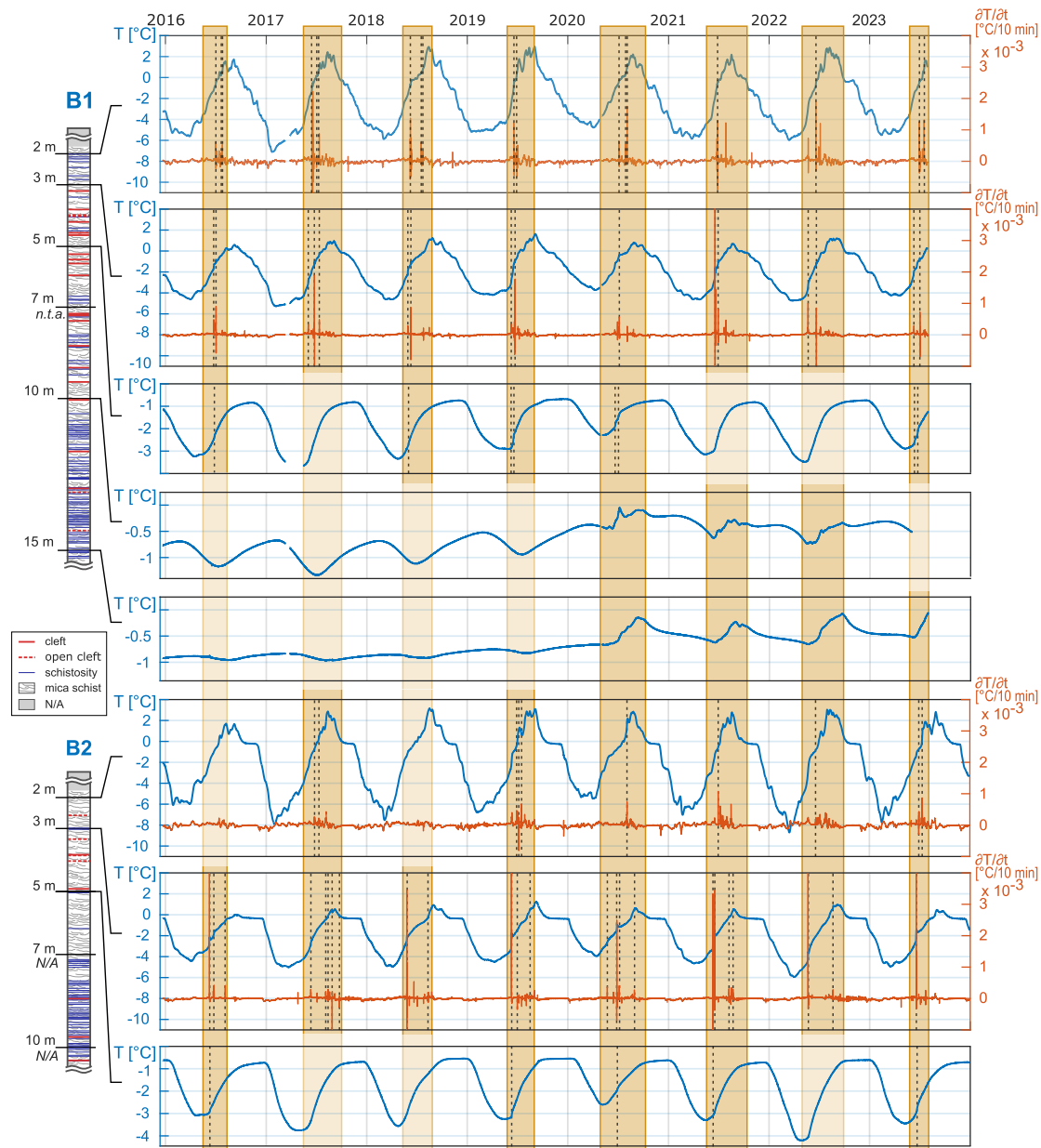
Figure 6. Thermal anomalies in rock temperature throughout the observation period (2016-2023): identified at 2 and 3 m depth (B1, B2) by abrupt changes using the first deviation with a moving average of a sample window size of 2 hours, and by irregularities and changes in the quasi-sinusoidal pattern observed in greater depths (B1: 5, 10, 15 m, B2: 5 m). Dashed lines mark an event of thermal disturbance, which mainly occurred between May and September. Thermistors showing no thermal anomalies (n.t.a.) or damage (N/A) are indicated accordingly.

Most of the thermal anomalies result in the warming of the rock mass, while only two events in August and September 2017 induced cooling in B2 at depths of 3 m. The initial rock temperature shortly before rapid changes at 2 and 3 m depth (B1 and B2) indicates that the push-like warming and cooling events were recorded mostly during frozen conditions of the surrounding rock mass (72 % of thermal anomalies, Fig. C1).

5 Discussion

5.1 Pressurised water flow in permafrost rockwalls

The unique time series of laboratory-calibrated ERT observations presented in this paper enable a quantitative interpretation of seasonal changes in frozen rockwalls. High-resistivity sections above 19 kΩm indicate frozen conditions with ice-filled joints during the frost season (October-May). Slight warming of the rock surface after the snow cover disappears in late spring is indicated by decreasing resistivity at shallow depth (e.g., tomography from June 2023 in Fig. 4). Ice-filled joints probably act as an aquitard, constraining deep infiltration into the joint system, with snowmelt mainly draining along the rock surface. From June to July, rapid changes in resistivity of more than one order of magnitude were observed at $\sim 1-7$ m depth coincident with a borehole temperature warming accompanied by active layer deepening from 1.7 to 2.7 m depth between the ERT measurement dates in June and July (Fig. 7a). The low resistivity zone (~ 4 kΩm) in July in the lower part of the
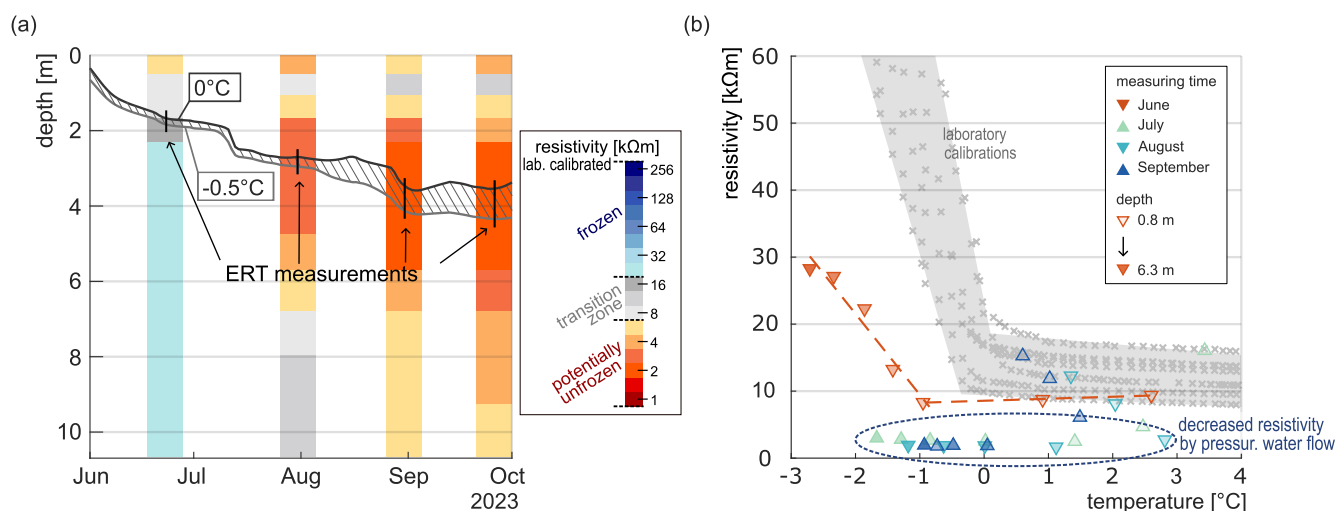
Figure 7. (a) Median resistivity values of the ERT measurements from June-September 2023, respectively, over the depth of the inverted blocks and the corresponding temporal evolution of the 0 °C/−0.5 °C observed in B2. Isotherms were calculated using average temperatures at 0.1 m depth over 3 days to minimize short-term fluctuations. (b) The resistivity-temperature relation of the field and laboratory ERT measurements showed a decrease in resistivity values from ~ -2 to 3 °C obtained between July and September.

tomography ($\sim$ electrodes 15-30) gradually expands to higher rock slope sections (Fig. 4) and to the bottom of the ERT profile until September ($\sim$ 10 m depth, Fig. 7a), while the 0 °C/−0.5 °C isotherm (i.e., permafrost table) changes marginally

(Aug: 3.5/4.1 m, Sep: 3.5/4.3 m). Comparing the temperature-resistivity relation observed in the field and in the laboratory

265   (Fig. 7b), the June ERT measurement shows resistivity values ($\sim$ 10 kΩm) above the equilibrium freezing point (> 0.2 °C) in the same range of laboratory calibrations, and the characteristic steeper resistivity-temperature gradient below the equilibrium freezing point (< −0.4 °C). However, the measured resistivity values from July to September exhibit decreasing values compared to laboratory calibrations from −2 to 3 °C with values < 10 kΩm. Even if a freezing point depression of −0.5 °C is assumed (Fig. 3b), the observed massive decline in electrical resistivity from July to September (Fig. 4, 7) cannot be understood

270   by changes in Archie's law. Instead, we assume that the pressurised character of water flow with its widespread fluid injection into the fracture network is essential to explain the rapid electrical resistivity decline. The word 'pressurised' is used here in the sense of a piezometric head of a few meters. This is evident from significant water outflow from fractures and first piezometric measurements installed after the ERT observations in late summer 2023, showing piezometric heads of up to 8-9 m. In addition, the coincident rapid changes and irregularities in rock temperature (up to 15 m depth, Fig. 6) cannot be explained solely by

275   diffusive heat exchange (Noetzli et al., 2007; Krautblatter et al., 2010), but only by water flow in open fractures (Phillips et al., 2016), facilitating a thermal shortcut between the atmosphere and the subsurface (Hasler et al., 2011).

We hypothesize that water from snowmelt infiltrates in early summer along local joints and fractures. Joint set K2, which dips steeply to SW (Fig. 1), may play a particularly prominent role. K2 extends perpendicular to the dip direction of the studied rock slope, effectively collecting surface runoff and diverting it into the subsurface. There, it is most likely redistributed along

280   the schistosity of the local calcareous mica-schists, i.e., through open, surface-parallel joints that drain the infiltrated water to the base of the rock slope. This hypothesis provides a plausible explanation for the observed development of a low-resistivity zone in the lower half of the ERT tomography in July, in which water seeps through one prominent K2 joints with apertures around 5 cm (Fig. 8) and is then drained down-slope and pressurised up-slope along the schistosity in August and September. In addition to snowmelt, rainfall events can contribute to infiltration, potentially leading to short-term warming in the subsurface

285   related to non-conductive heat fluxes, and decreased resistivity. No rainfall has been registered in the days leading up to or during the ERT data acquisitions, so modifications of the hydrological regime through precipitation are not discussed here.

The results of this study underline the high impact of fluid flow in fractures on hydrological and thermal processes in alpine permafrost rockwalls. Due to its complexity and lack of knowledge, thermal models of permafrost distribution have often neglected the hydrology of rockwalls (e.g., Duvillard et al., 2021a; Etzelmüller et al., 2022), or have relied on an assumption

290   of weathered zones and high porosity to represent fracture density (e.g., Noetzli et al., 2007; Magnin et al., 2017), which does not fully describe the main effects of a fracture network on permeability characteristics in low porosity rock (Hsieh, 1998). However, fluid flow in fractures is often decisive for rapid changes in permafrost distribution in rockwalls as already shown by geophysical measurements (Krautblatter and Hauck, 2007; Krautblatter et al., 2010; Keuschnig et al., 2017; Magnin and Josnin, 2021), numerical approaches (Magnin and Josnin, 2021) and our combined analysis of long-term ERT monitoring

295   and borehole temperatures. As evidenced by several rapid drops in rock temperature recorded at the Kitzsteinhorn and at the Gemsstock borehole in Switzerland (Phillips et al., 2016), we suggest that fractures can act as cooling pathways, favoring the formation of freezing corridors. Ice-filled fractures initially cool the surrounding rock mass and prevent warm water infiltration. Still, as the melting of the basal ice layer begins, thaw corridors are formed, which initiate rapid non-conductive warming in
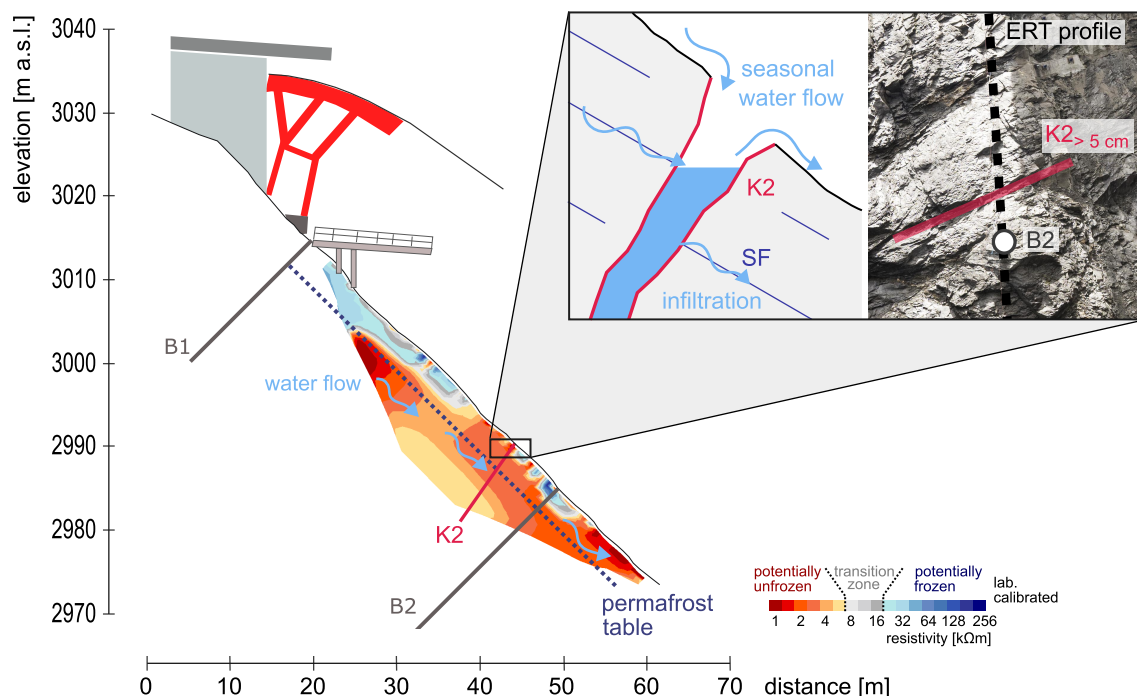
Figure 8. Conceptual illustration of water infiltration and flow along the schistosity (SF) and geotechnical discontinuities (e.g., fracture K2 with aperture of > 5 cm) using the ERT measurement from September 2023. Permafrost table is derived from temperature measurements at borehole B2.

spring/summer. Cooling in autumn/winter, on the other hand, is controlled by slow conductive heat transport and contributes

300   to the persistence of relatively warm areas at larger depths. This water-flow-induced seasonal succession of rapid warming and slow cooling results in a positive thermal offset, as observed in B1 and B2 (Fig. 5a), which, over long time periods, results in bottom-up oriented permafrost degradation.

5.2   Limitations and uncertainties

Laboratory calibrations are commonly applied to enable a quantitative interpretation of ERT monitoring in permafrost bedrock.

305   We carried out laboratory ERT measurements on unfrozen and frozen mica-schist rock samples, representative of the homogeneous lithology of the study side, with only a scaly band of serpentinite at a depth of approximately 15 m according to optical borehole scans. As the ERT measurements at the north flank reached a maximum penetration depth of around 10 m, serpentinite probes were not included in the laboratory experiments. A bilinear description of the resistivity-temperature relation was preferred over an exponential behavior of resistivity values below the freezing point, which is less appropriate for low-porosity

310   bedrock (Krautblatter et al., 2010) compared to freezing in unconfined space (e.g., debris) and requires more unknown input parameters (Duvillard et al., 2021a). Our results suggest frozen conditions above 19 kΩm and a frozen temperature-resistivity gradient of 44.9 ± 12.0 kΩm/ °C, comparable to laboratory calibrations of rocks with different lithologies (Krautblatter et al.,

2010; Magnin et al., 2015; Scandroglio et al., 2021; Etzelmüller et al., 2022). However, the problem of extrapolating from laboratory experiments to field observations (Zisser et al., 2007; Krautblatter et al., 2010) was highlighted by our ERT observation of the highly fractured rock face, which indicated the strong influence of water-saturated fractures and cracks on the electrical properties, less represented by the intact rock mass of the laboratory studies.

Sources of error in geophysical models are associated with data acquisition and subsequent inversion. Keuschnig et al. (2017) indicated that wind gusts, especially above 10 m/s, might induce measurement errors. Here, we only used ERT measurements from 2013 and 2023, carried out during periods with wind speeds below 10 m/s, making additional pre-filtering superfluous. The penetration depth of the current flow into the subsurface depends on the characteristics of the top layer and may vary seasonally. Dry and frozen conditions can impede current flow, while water-saturated conditions might trap current flow, resulting in an attenuated current flow into deeper layers (Loke, 2022). Poor electrode coupling is often associated with frozen conditions and ice-filled fractures and cracks from autumn to spring, which cause noisy data and can lead to inversion artifacts represented by a high RMS error. Consequently, we refrained from detailed interpretation of the inverted tomograms from February to May 2013 and September to December. In addition, we analyzed the raw data from June to September 2023 to exclude an inappropriate choice of inversion parameters, even though the tomograms exhibit a marginal RMS error of less than 4.3 %. The apparent resistivity values indicate a decreasing trend over the summer (Fig. B2), consistent with the patterns shown by the respective inverted tomograms.

Borehole temperature measurements are vulnerable to lightning strikes, leading to sporadic thermistor failures, as happened in several depths (0.5, 7, 10, 20, 25 m) in B2 between 2017-2023. Therefore, the frequency of thermal anomalies recorded in B2 may be underrepresented. The overall record of thermal anomalies, however, is derived from a seven-year dataset (2016-2023) and in numerous depths (B1: 2, 3, 5, 7, 10, 15 m, B2: 2, 3, 5 m), still holds high significance. The system used for borehole temperature measurement facilitates direct physical contact between sensors and ambient rock mass and is, therefore, ideally suited to record short-term temperature changes. However, despite their high sensitivity, the measured thermal signals are assumed to be considerably damped compared to direct temperature measurements in fractures or cracks. Actual temperature jumps induced by water flow in fractures are expected to be significantly higher than the ones measured inside B1 and B2.

5.3 Implications for rock wall instabilities and permafrost monitoring

Understanding water flow in fractured permafrost rocks is challenging but crucial to improving process knowledge of permafrost dynamics. The interaction between fracture fills of air, water and ice, and the surrounding bedrock results in complex thermal patterns that strongly influence permafrost evolution and have further implications for the mechanical rock regime.

High, seasonally varying displacement rates of rock slope instabilities (Wirz et al., 2014; Mamot et al., 2021; Etzelmüller et al., 2022) and irreversible fracture displacements in summer (Weber et al., 2017) have already been linked to thawing-related processes such as meltwater infiltration in cracks and fractures. Induced hydraulic and/or hydrostatic pressures may induce uplift, which reduces the effective normal stress and thus the shear resistance (Wyllie, 2017), and can contribute as a triggering factor to slope failures in alpine rocks (Fischer et al., 2010; Walter et al., 2020; Kristensen et al., 2021). Our results

show that repeated ERT monitoring can detect water infiltration and is, therefore, a promising approach to identify periods with high hydrostatic pressure relevant for slope stability assessment.

Abrupt temperature changes recorded in B1 and B2, mainly during periods of subzero temperature (Fig. C1), indicate non-conductive heat fluxes. These sudden push-like events can transport heat from the surface to greater depths more rapidly than slow thermal conduction, which is consistent with laboratory experiments by Hasler et al. (2011). The induced temperature rise may lead to slope destabilization, as warming and thawing processes alter the shear resistance of ice-filled rock joints (Gruber and Haeberli, 2007; Mamot et al., 2018) and affect the rock-ice mechanics of permafrost slopes (Krautblatter et al., 2013).

Monitoring of alpine permafrost often relies solely on annually repeated geoelectric measurements, mainly due to complicated logistics and harsh measurement conditions. However, our study suggests that higher ERT measurement intervals are required to decipher the complexity of hydrothermal processes in permafrost rockwalls and fully assess the rate and extent of permafrost evolution. Monthly ERT measurements in this contribution represent a significant advancement compared to annual surveys. Concerning the transient nature of water flux in rock slope systems, daily or hourly measurements would represent another significant step towards a better understanding of water flow in fractures. Furthermore, we emphasize the key role of complementary temperature measurements and their joint analysis. Low electrical resistivity values in the absence of borehole temperatures may be misinterpreted as permafrost-free rock slopes, yet. They could serve as an indicator of water-saturated conditions above a potential permafrost body.

6 Conclusions

The role of water flow in permafrost rockwalls is rarely investigated and remains a key challenge. This study proposes an approach to infer water flow in bedrock permafrost by combining monthly repeated electrical resistivity monitoring and long-term temperature measurements in deep boreholes. The following conclusions are drawn:

1. We observed a massive decrease in electrical resistivity from June to July, which extends to deeper layers an higher rock slope sections until September. During the freezing period, ice-filled joints probably prevent water from infiltrating the rock and initially cool the surrounding rock mass. With the melting of the basal ice layer and the formation of thaw corridors in spring, we hypothesize that snowmelt water infiltrates the rockwall and is subsequently drained along the schistosity and interconnected joints to the base of the rock slope. Throughout the summer, the water flow is pressurised into a widespread fracture network.

2. Small, abrupt temperature changes registered in two boreholes between May and September indicate non-conductive heat flux in fractures. Frozen rock is warmed more rapidly by these sudden push-like events of heat transport from the surface than by slow thermal conduction alone.

3. Permafrost evolution in low-porosity bedrock is highly dependent on fracturing and the course of the schistosity, which can induce bottom-up permafrost degradation.

4. High hydrostatic pressure potentially alters slope stability. Our results show that enhanced ERT monitoring can potentially identify critical, water-saturated zones with high hydrostatic pressure.

This study has broad implications for understanding hydrothermal processes in steep, fractured rock walls, the rate and extent
380   of permafrost degradation, and related hazards. Future developments are needed to validate and quantify our observations. Of
particular interest would be the inclusion of piezometric information and temperature measurements within fractures.

Appendix A: Resistivity-temperature laboratory calibration

Table A1. Fitting parameters of the bilinear relationship between resistivity and temperature data below and above the equilibrium freezing point T_f of the laboratory experiments.

	T_f	below T_f			above T_f		
		a	b	R^2	a	b	R^2
S1-1	0.22	23.6	-48.7	0.99	13.2	-0.6	0.77
S1-2	-0.24	2.9	-56.9	0.99	16.3	-0.7	0.93
S2-1	-0.35	-2.0	-32.8	0.99	9.6	-0.4	0.91
S2-2	-0.26	7.7	-34.6	1.00	16.5	-0.8	0.83
S3-1	-0.31	1.0	-33.6	1.00	11.3	-0.5	0.79
S3-2	-0.06	13.1	-35.3	1.00	15.3	-0.7	0.82
S3-3	0.07	22.6	-48.7	1.00	19.0	-0.8	0.76

Table B1. Detailed information on the ERT measurement procedures and inversion routines.

	2013					2023				2013		
	Feb	Mar	Apr	May	June	June	July	Aug	Sep	Sep	Oct	Nov	Dec
Date	28th	26th	28th	28th	16th	23th	31st	31st	26th	27th	08th	28th	28th
Device	Geo-Tom-MK1E100					ABEM terrameter LS				Geo-Tom-MK1E100			
Output current [mA]	0.001 - 200					0.1 - 2500				0.001 - 200			
Voltage max [V]	500					600				500V			
Filtering current effects [Hz]	16 2/3, 50, 60					50				16 2/3, 50, 60			
Stacks	3					2-4				3			
No. of outliers/	2/	1/	1/	1/	1/	-/	-/	-/	-/	-/	-/	3/	1/
inverted datum points	133	134	134	134	134	135	135	135	135	135	135	132	134
Iterations	5	5	5	5	5	5	5	5	5	4	5	4	3
RMS error [%]	53.0	32.7	18.9	12.7	12.0	4.3	3.6	3.8	4.2	30.7	2.1	55.2	53.2

Appendix B: ERT monitoring
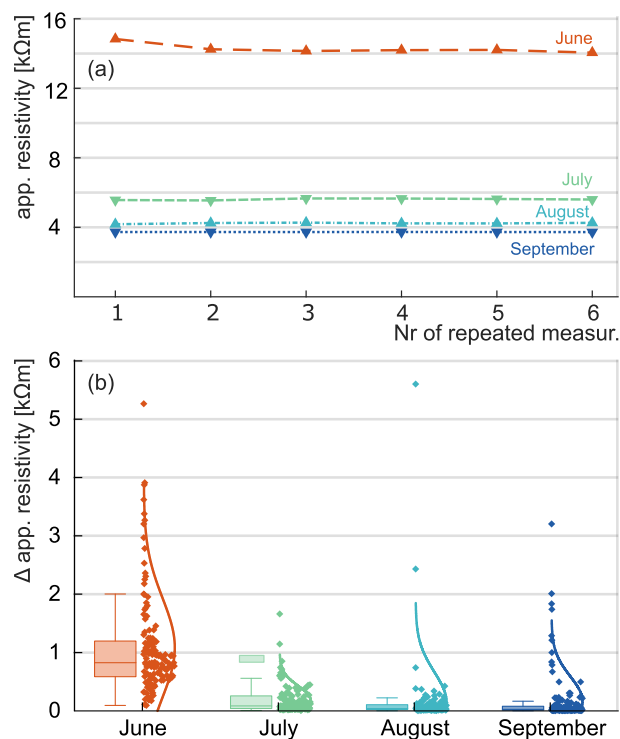
Figure B1. Short-term variations in apparent resistivity during repeated ERT measurements (June-September 2023) over a 24-hour period. (a) Median apparent resistivity values indicate relatively stable conditions over an observation period, which is additionally supported by (b) the maximum difference in apparent resistivity of respective datum points (n=135) over repeated ERT measurements, mostly less than 2 kΩm.
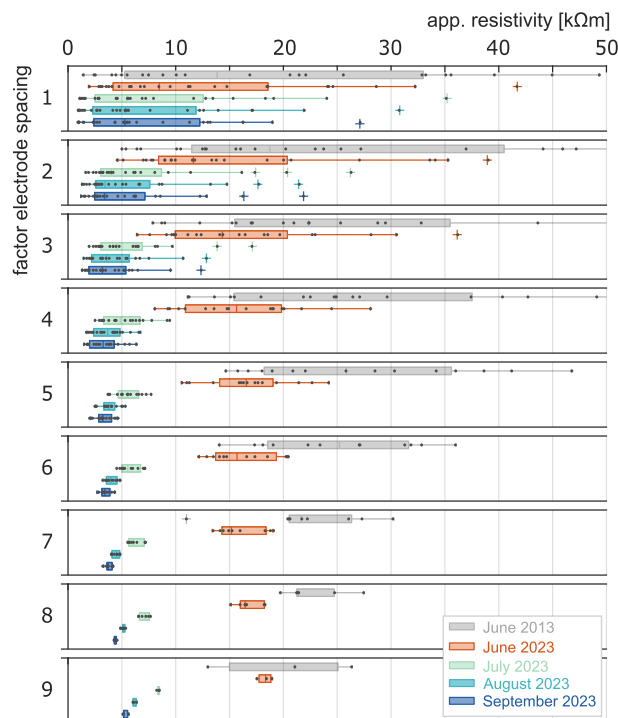
Figure B2. Statistical box plots with jitter data points of the apparent resistivity of the ERT measurements in June 2013 and from June to September 2023 with respect to the distance between the electrodes. It should be noted that as the electrode spacing factor increases, fewer values are measured.
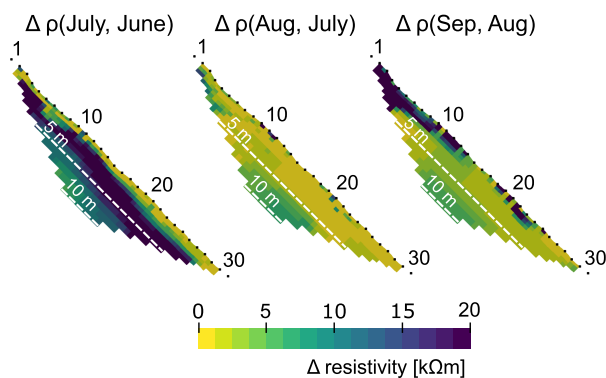
Figure B3. Difference in resistivity between tomograms observed from June-July (left), July-August (middle), and August-September (right) in 2023. Significant decreases in electrical resistivity values are evident at greater depths (~2-7 m) between June-July, while resistivity values remain relatively stable with only slight changes (< 10 kΩm) between July-September.

Appendix C: Abrupt changes in borehole temperature
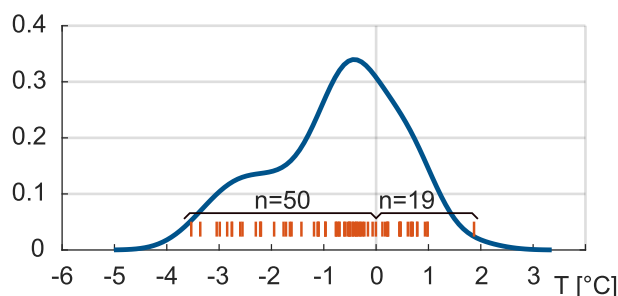
Figure C1. Kernel distribution of rock temperature at 2 and 3 m depth (B1, B2) prior to registered thermal anomalies: Most rapid warming or cooling events (anomalies) occurred at subzero temperature.

385   *Data availability.*   Data will be made available on request.

Author contributions.   MO wrote the manuscript, conducted the geophysical surveys in 2023, performed the data analysis and designed the figures with substantial contribution from SW and MKe. MKe provided the data sets of geophysical surveys in 2013 and IH contributed borehole temperature data. SW, MKr and MKe supervised the study. All authors contributed to the interpretation of the results and improved the final version of the manuscript.

390   *Competing interests.*   The authors declare that they have no conflict of interest.

Acknowledgements.   Maike Offer acknowledges PhD funding from the Deutsche Bundesstiftung Umwelt (DBU). The authors would like to thank Maximilian Rau, Felix Pfluger, Georg Stockinger, and Maximilian Reinhard for their extensive support during the fieldwork. We furthermore thank the Gletscherbahnen Kaprun AG (Project 'Open-Air-Lab Kitzsteinhorn') for financial and logistical support.

References

395 Arenson, L. U., Harrington, J. S., Koenig, C. E. M., and Wainstein, P. A.: Mountain Permafrost Hydrology—A Practical Review Following Studies from the Andes, Geosciences, 12, 48, https://doi.org/10.3390/geosciences12020048, 2022.

Bast, A., Kenner, R., and Phillips, M.: Short-term cooling, drying and deceleration of an ice-rich rock glacier, EGUsphere [preprint], https://doi.org/10.5194/egusphere-2024-269, 2024.

Buckel, J., Mudler, J., Gardeweg, R., Hauck, C., Hilbich, C., Frauenfelder, R., Kneisel, C., Buchelt, S., Blöthe, J. H., Hördt, A., and Bücker,
400 M.: Identifying mountain permafrost degradation by repeating historical electrical resistivity tomography (ERT) measurements, The Cryosphere, 17, 2919–2940, https://doi.org/10.5194/tc-17-2919-2023, 2023.

Cathala, M., Magnin, F., Ravanel, L., Dorren, L., Zuanon, N., Berger, F., Bourrier, F., and Deline, P.: Mapping release and propagation areas of permafrost-related rock slope failures in the French Alps: A new methodological approach at regional scale, Geomorphology, 448, 109 032, https://doi.org/10.1016/j.geomorph.2023.109032, 2024.

405 Cimpoiasu, M. O., Kuras, O., Harrison, H., Wilkinson, P. B., Meldrum, P., Chambers, J. E., Liljestrand, D., Oroza, C., Schmidt, S. K., Sommers, P., Vimercati, L., Irons, T. P., Lyu, Z., Solon, A., and Bradley, J. A.: High-resolution 4D ERT monitoring of recently deglaciated sediments undergoing freeze-thaw transitions in the High Arctic, EGUsphere [preprint], https://doi.org/10.5194/egusphere-2024-350, 2024.

Cornelius, H. P. and Clar, E.: Erläuterungen zur geologischen Karte des Glocknergebietes, 1935.

Draebing, D. and Krautblatter, M.: P-wave velocity changes in freezing hard low-porosity rocks: a laboratory-based time-average model, The
410 Cryosphere, 6, 1163–1174, https://doi.org/10.5194/tc-6-1163-2012, 2012.

Duvillard, P.-A., Ravanel, L., Marcer, M., and Schoeneich, P.: Recent evolution of damage to infrastructure on permafrost in the French Alps, Reg. Environ. Change, 19, 1281–1293, https://doi.org/10.1007/s10113-019-01465-z, 2019.

Duvillard, P.-A., Magnin, F., Revil, A., Legay, A., Ravanel, L., Abdulsamad, F., and Coperey, A.: Temperature distribution in a permafrost-affected rock ridge from conductivity and induced polarization tomography, Geophys. J. Int., 225, 1207–1221,
415 https://doi.org/10.1093/gji/ggaa597, 2021a.

Duvillard, P.-A., Ravanel, L., Schoeneich, P., Deline, P., Marcer, M., and Magnin, F.: Qualitative risk assessment and strategies for infrastructure on permafrost in the French Alps, Cold Reg. Sci. Technol., 189, 103 311, https://doi.org/10.1016/j.coldregions.2021.103311, 2021b.

Etzelmüller, B., Guglielmin, M., Hauck, C., Hilbich, C., Hoelzle, M., Isaksen, K., Noetzli, J., Oliva, M., and Ramos, M.: Twenty years of European mountain permafrost dynamics—the PACE legacy, Environ. Res. Lett., 15, 104 070, https://doi.org/10.1088/1748-9326/abae9d,
420 2020.

Etzelmüller, B., Czekirda, J., Magnin, F., Duvillard, P.-A., Ravanel, L., Malet, E., Aspaas, A., Kristensen, L., Skrede, I., Majala, G. D., Jacobs, B., Leinauer, J., Hauck, C., Hilbich, C., Böhme, M., Hermanns, R., Eriksen, H. Ø., Lauknes, T. R., Krautblatter, M., and Westermann, S.: Permafrost in monitored unstable rock slopes in Norway – new insights from temperature and surface velocity measurements, geophysical surveying, and ground temperature modelling, Earth Surf. Dynam., 10, 97–129, https://doi.org/10.5194/esurf-10-97-2022, 2022.

425 Fischer, L., Amann, F., Moore, J. R., and Huggel, C.: Assessment of periglacial slope stability for the 1988 Tschierva rock avalanche (Piz Morteratsch, Switzerland), Eng. Geol., 116, 32–43, https://doi.org/10.1016/j.enggeo.2010.07.005, 2010.

Gruber, S. and Haeberli, W.: Permafrost in steep bedrock slopes and its temperature-related destabilization following climate change, J. Geophys. Res., 112, F02S18, https://doi.org/10.1029/2006JF000547, 2007.

Gruber, S., King, L., Kohl, T., Herz, T., Haeberli, W., and Hoelzle, M.: Interpretation of geothermal profiles perturbed by to-
pography: the alpine permafrost boreholes at Stockhorn Plateau, Switzerland, Permafrost and Periglac. Process., 15, 349–357,
https://doi.org/10.1002/ppp.503, 2004.

Hartmeyer, I., Keuschnig, M., and Schrott, L.: Long-term monitoring of permafrost-affected rock faces—A scale-oriented approach for the
investigation of ground thermal conditions in alpine terrain, Kitzsteinhorn, Austria, Austrian J. Earth Sc., 105, 128–139, 2012.

Hartmeyer, I., Delleske, R., Keuschnig, M., Krautblatter, M., Lang, A., Schrott, L., and Otto, J.-C.: Current glacier recession causes
significant rockfall increase: the immediate paraglacial response of deglaciating cirque walls, Earth Surf. Dynam., 8, 729–751,
https://doi.org/10.5194/esurf-8-729-2020, 2020.

Hasler, A., Gruber, S., Font, M., and Dubois, A.: Advective Heat Transport in Frozen Rock Clefts: Conceptual Model, Laboratory Experi-
ments and Numerical Simulation, Permafrost and Periglac. Process., 22, 378–389, https://doi.org/10.1002/ppp.737, 2011.

Hauck, C.: Frozen ground monitoring using DC resistivity tomography, Geophys. Res. Lett., 29, 12–1–12–4,
https://doi.org/10.1029/2002GL014995, 2002.

Hauck, C. and Kneisel, C., eds.: Applied Geophysics in periglacial environments, Cambirge University Press, 2008.

Herring, T., Lewkowicz, A. G., Hauck, C., Hilbich, C., Mollaret, C., Oldenborger, G. A., Uhlemann, S., Farzamian, M., Calmels, F., and
Scandroglio, R.: Best practices for using electrical resistivity tomography to investigate permafrost, Permafrost and Periglac. Process., 34,
494–512, https://doi.org/10.1002/ppp.2207, 2023.

Hilbich, C.: Time-lapse refraction seismic tomography for the detection of ground ice degradation, The Cryosphere, 4, 243–259,
https://doi.org/10.5194/tc-4-243-2010, 2010.

Hilbich, C., Hauck, C., Mollaret, C., Wainstein, P., and Arenson, L. U.: Towards accurate quantification of ice content in per-
mafrost of the Central Andes – Part 1: Geophysics-based estimates from three different regions, The Cryosphere, 16, 1845–1872,
https://doi.org/10.5194/tc-16-1845-2022, 2022.

Hoeck, V., Pestal, G., Brandmaier, P., Clar, E., Cornelius, H., Frank, W., Matl, H., Neumayr, P., Petrakakis, K., Stadlmann, T., and Steyrer,
H.: Geologische Karte der Republik Österreich: Blatt 153 Großglockner, 1994.

Hsieh, P. A.: Scale effects in fluid flow through fractured geologic media, in: Scale dependence and scale invariance in hydrology, edited by
Sposito, G., pp. 335–353, Cambridge Univ. Press, Cambridge, https://doi.org/10.1017/CBO9780511551864.013, 1998.

Keuschnig, M., Hartmeyer, I., Otto, J.-C., and Schrott, L.: A new permafrost and mass movement monitoring test site in the Eastern
Alps–concept and first results of the MOREXPERT project, in: Managing Alpine future II—inspire and drive sustainable mountain
regions, edited by Borsdorf, A., Stötter, J., and Veulliet, E., Proceedings of the Innsbruck Conference, 21–23 November 2011. (=IGF-
Forschungsberichte 4)., Verlag der Österreichischen Akademie der Wissenschaften, Vienna, 2011.

Keuschnig, M., Krautblatter, M., Hartmeyer, I., Fuss, C., and Schrott, L.: Automated Electrical Resistivity Tomography Testing for
Early Warning in Unstable Permafrost Rock Walls Around Alpine Infrastructure, Permafrost and Periglac. Process., 28, 158–171,
https://doi.org/10.1002/ppp.1916, 2017.

Krautblatter, M. and Hauck, C.: Electrical resistivity tomography monitoring of permafrost in solid rock walls, J. Geophys. Res., 112, F02S20,
https://doi.org/10.1029/2006JF000546, 2007.

Krautblatter, M., Verleysdonk, S., Flores-Orozco, A., and Kemna, A.: Temperature-calibrated imaging of seasonal changes in per-
mafrost rock walls by quantitative electrical resistivity tomography (Zugspitze, German/Austrian Alps), J. Geophys. Res., 115, F02003,
https://doi.org/10.1029/2008JF001209, 2010.

Krautblatter, M., Huggel, C., Deline, P., and Hassler, A.: Research perspectives on unstable high-alpine bedrock permafrost: measurement, modelling and process understanding, Permafrost and Periglac. Process., 23, 80–88, https://doi.org/10.1002/ppp.740, 2012.

Krautblatter, M., Funk, D., and Günzel, F. K.: Why permafrost rocks become unstable: a rock-ice-mechanical model in time and space, Earth Surf. Process. Landforms, 38, 876–887, https://doi.org/10.1002/esp.3374, 2013.

470 Kristensen, L., Czekirda, J., Penna, I., Etzelmüller, B., Nicolet, P., Pullarello, J. S., Blikra, L. H., Skrede, I., Oldani, S., and Abellan, A.: Movements, failure and climatic control of the Veslemannen rockslide, Western Norway, Landslides, 18, 1963–1980, https://doi.org/10.1007/s10346-020-01609-x, 2021.

Krus, M.: Feuchtetransport und Speicherkoeffizienten poröser mineralischer Baustoffe - theoretische Grundlagen und neue Meßtechniken., dissertation, University of Stuttgart, Faculty of Civil and Environmental Engineering, 1995.

475 Loke, M. H.: Tutorial: 2-D and 3-D electrical imaging surveys, 2022.

Loke, M. H. and Barker, R. D.: Rapid least–squares inversion of apparent resistivity pseudosections by a quasi–Newton method, Geophysical Prospecting, 44, 131–152, https://doi.org/10.1111/j.1365-2478.1996.tb00142.x, 1996.

Magnin, F. and Josnin, J.-Y.: Water Flows in Rock Wall Permafrost: A Numerical Approach Coupling Hydrological and Thermal Processes, J. Geophys. Res. Earth Surface, 126, e2021JF006394, https://doi.org/10.1029/2021JF006394, 2021.

480 Magnin, F., Deline, P., Ravanel, L., Noetzli, J., and Pogliotti, P.: Thermal characteristics of permafrost in the steep alpine rock walls of the Aiguille du Midi (Mont Blanc Massif, 3842 m a.s.l.), The Cryosphere, 9, 109–121, https://doi.org/10.5194/tcd-8-2831-2014, 2015.

Magnin, F., Josnin, J.-Y., Ravanel, L., Pergaud, J., Pohl, B., and Deline, P.: Modelling rock wall permafrost degradation in the Mont Blanc massif from the LIA to the end of the 21st century, The Cryosphere, 11, 1813–1834, https://doi.org/10.5194/tc-11-1813-2017, 2017.

Mamot, P., Weber, S., Schröder, T., and Krautblatter, M.: A temperature- and stress-controlled failure criterion for ice-filled permafrost rock

485 joints, The Cryosphere, 12, 3333–3353, https://doi.org/10.5194/tc-12-3333-2018, 2018.

Mamot, P., Weber, S., Lanz, M., and Krautblatter, M.: Brief communication: The influence of mica-rich rocks on the shear strength of ice-filled discontinuities, The Cryosphere, 14, 1849–1855, https://doi.org/10.5194/tc-14-1849-2020, 2020.

Mamot, P., Weber, S., Eppinger, S., and Krautblatter, M.: A temperature-dependent mechanical model to assess the stability of degrading permafrost rock slopes, Earth Surf. Dynam., 9, 1125–1151, https://doi.org/10.5194/esurf-9-1125-2021, 2021.

490 Mollaret, C., Hilbich, C., Pellet, C., Flores-Orozco, A., Delaloye, R., and Hauck, C.: Mountain permafrost degradation documented through a network of permanent electrical resistivity tomography sites, The Cryosphere, 13, 2557–2578, https://doi.org/10.5194/tc-13-2557-2019, 2019.

Noetzli, J., Gruber, S., Kohl, T., Salzmann, N., and Haeberli, W.: Three–dimensional distribution and evolution of permafrost temperatures in idealized high–mountain topography, J. Geophys. Res., 112, https://doi.org/10.1029/2006JF000545, 2007.

495 Outcalt, S. I., Nelson, F. E., and Hinkel, K. M.: The zero–curtain effect: Heat and mass transfer across an isothermal region in freezing soil, Water Resour. Res., 26, 1509–1516, https://doi.org/10.1029/WR026i007p01509, 1990.

Phillips, M., Haberkorn, A., Draebing, D., Krautblatter, M., Rhyner, H., and Kenner, R.: Seasonally intermittent water flow through deep fractures in an Alpine Rock Ridge: Gemsstock, Central Swiss Alps, Cold Reg. Sci. Technol., 125, 117–127, https://doi.org/10.1016/j.coldregions.2016.02.010, 2016.

500 Phillips, M., Buchli, C., Weber, S., Boaga, J., Pavoni, M., and Bast, A.: Brief communication: Combining borehole temperature, borehole piezometer and cross-borehole electrical resistivity tomography measurements to investigate seasonal changes in ice-rich mountain permafrost, The Cryosphere, 17, 753–760, https://doi.org/10.5194/tc-17-753-2023, 2023.

Pogrebiskiy, M. and Chernyshev, S.: Determination of the permeability of the frozen fissured rock massif in the vicinity of the Kolyma hydroelectric power station, Cold Regions Research and Engineering Laboratory – Draft Translation, 634, 1–13, 1977.

505 Ravanel, L., Magnin, F., and Deline, P.: Impacts of the 2003 and 2015 summer heatwaves on permafrost-affected rock-walls in the Mont Blanc massif, Sci. Total Environ., 609, 132–143, https://doi.org/10.1016/j.scitotenv.2017.07.055, 2017.

Sass, O.: Die Steuerung von Steinschlagmenge und –verteilung durch Mikroklima, Gesteinsfeuchte und Gesteinseigenschaften im westlichen Karwendelgebirge (Bayerische Alpen), Münchener Geographische Abhandlungen, pp. 1–175, 1998.

Savi, S., Comiti, F., and Strecker, M. R.: Pronounced increase in slope instability linked to global warming: A case study from the eastern
510 European Alps, Earth Surf. Process. Landforms, 46, 1328–1347, https://doi.org/10.1002/esp.5100, 2021.

Scandroglio, R., Draebing, D., Offer, M., and Krautblatter, M.: 4D quantification of alpine permafrost degradation in steep rock walls using a laboratory–calibrated electrical resistivity tomography approach, Near Surface Geophys., 19, 241–260, https://doi.org/10.1002/nsg.12149, 2021.

Schneider, S., Daengeli, S., Hauck, C., and Hoelzle, M.: A spatial and temporal analysis of different periglacial materials by using
515 geoelectrical, seismic and borehole temperature data at Murtèl–Corvatsch, Upper Engadin, Swiss Alps, Geogr. Helv., 68, 265–280, https://doi.org/10.5194/gh-68-265-2013, 2013.

Schober, A., Bannwart, C., and Keuschnig, M.: Rockfall modelling in high alpine terrain - validation and limitations / Steinschlagsimulation in hochalpinem Raum - Validierung und Limitationen, Geomechanics and Tunnelling, 5, 368–378, https://doi.org/10.1002/geot.201200025, 2012.

520 Schrott, L., Otto, J.-C., and Keller, F.: Modelling alpine permafrost distribution in the Hohe Tauern region, Austria, Austrian J. Earth Sc., 105, 169–183, 2012.

Telford, W. M., Geldart, L. P., and Sheriff, R. E.: Applied geophysics, Cambridge Univ. Pr, Cambridge, 2 edn., 2004.

Wagner, F. M., Mollaret, C., Günther, T., Kemna, A., and Hauck, C.: Quantitative imaging of water, ice and air in permafrost systems through petrophysical joint inversion of seismic refraction and electrical resistivity data, Geophys. J. Int., 219, 1866–1875,
525 https://doi.org/10.1093/gji/ggz402, 2019.

Walter, F., Amann, F., Kos, A., Kenner, R., Phillips, M., de Preux, A., Huss, M., Tognacca, C., Clinton, J., Diehl, T., and Bonanomi, Y.: Direct observations of a three million cubic meter rock-slope collapse with almost immediate initiation of ensuing debris flows, Geomorphology, 351, 106 933, https://doi.org/10.1016/j.geomorph.2019.106933, 2020.

Weber, S., Beutel, J., Faillettaz, J., Hasler, A., Krautblatter, M., and Vieli, A.: Quantifying irreversible movement in steep, fractured bedrock
530 permafrost on Matterhorn (CH), The Cryosphere, 11, 567–583, https://doi.org/10.5194/tc-11-567-2017, 2017.

Weber, S., Fäh, D., Beutel, J., Faillettaz, J., Gruber, S., and Vieli, A.: Ambient seismic vibrations in steep bedrock permafrost used to infer variations of ice-fill in fractures, Earth Planet. Sc. Lett., 501, 119–127, https://doi.org/10.1016/j.epsl.2018.08.042, 2018.

Wirz, V., Beutel, J., Gruber, S., Gubler, S., and Purves, R. S.: Estimating velocity from noisy GPS data for investigating the temporal variability of slope movements, Nat. Hazards Earth Syst. Sci., 14, 2503–2520, https://doi.org/10.5194/nhess-14-2503-2014, 2014.

535 Wyllie, D. C., ed.: Rock slope engineering, CRC Press, 5 edn., 2017.

Zhou, B. and Dahlin, T.: Properties and effects of measurement errors on 2D resistivity imaging surveying, Near Surface Geophys., 1, 105–117, https://doi.org/10.3997/1873-0604.2003001, 2003.

Zisser, N., Nover, G., Dürrast, H., and Siegesmund, S.: Relationship between electrical and hydraulic properties of sedimentary rocks, Z. dt. Ges. Geowiss., 158, 883–894, https://doi.org/10.1127/1860-1804/2007/0158-0883, 2007.